

# *Ab Initio* Photon-Electron and Electron-Vibration Coupling Calculations Related to Laser Cooling of Ion-Doped Solids

X. L. Ruan<sup>†</sup> and M. Kaviany\*

Department of Mechanical Engineering, University of Michigan, Ann Arbor, MI 48105, USA

An *ab initio* approach is developed to determine the photon-electron and electron-vibration coupling rates, for ion-doped materials related to laser cooling of solids. The ground and excited state energies are determined, and the corresponding geometries optimized. Using the first-principle wavefunctions, the electric transition dipole moment connecting the ground and excited states is calculated, and is found to be highly dependent on the symmetry properties of the system. The electron-phonon coupling is caused by the modification of the electronic wavefunction in response to the nuclei motions, and by the modifications of the vibrational modes before and after the transition. This theory is used to calculate the nonradiative decay rate, which is strongly dependent on the temperature. Based on such an understanding of the photon-electron and electron-vibration coupling physics, the optimal selection of laser cooling materials is discussed.

**Keywords:** Laser Cooling, First Principles, Photon-Electron Coupling, Electron-Vibration Coupling.

## 1. INTRODUCTION

The concept of laser cooling (optical refrigeration) of solids dates back to 1929, when Pringsheim recognized that thermal vibrational energy (phonon) can be removed by the anti-Stokes fluorescence, i.e., the photons emitted by an optical material have a mean energy higher than that of the absorbed photons.<sup>1</sup> Initially, it was believed that optical cooling by the anti-Stokes fluorescence contradicted the second law of thermodynamics. Predictions suggested that the cycle of excitation and fluorescence was reversible, and hence the optical cooling would be equivalent to the complete transformation of heat to work.<sup>2,3</sup> This issue was cleared by Landau by assigning entropy to radiation.<sup>4</sup> It was shown that the entropy of a radiation field increases with its frequency bandwidth and also the solid angle through which it propagates. Since the incident laser light has a very small bandwidth and propagates in a well-defined direction, it has almost zero entropy. On the other hand, the fluorescence is relatively broadband and is emitted in all directions, and therefore, it has a comparatively larger entropy. In this way, the second law of thermodynamics is satisfied.

Many attempts have been made to realize radiative refrigeration experimentally, and the associated theoretical interpretations have been discussed. The earliest experiment was performed by Kushida and Geusic on Nd:YAG.<sup>5</sup> Reduced heating other than net cooling was observed, which was conjectured to be a result of the impurities in the crystal. Later Djeu and Whitney laser cooled low-pressure CO<sub>2</sub> by 1 K from 600 K by using a CO<sub>2</sub> laser for pumping.<sup>6</sup> In 1995, Epstein et al.<sup>7</sup> reported the first successful experiment of laser cooling in solids. Since then, various Yb or Tm doped glasses and crystals have been cooled.<sup>8–17</sup> Particularly, bulk solids have been cooled from room temperature to 208 K (creating a temperature difference  $\Delta T = 92$  K).<sup>17</sup> Continuous progress has been made<sup>15,18,19</sup> towards achieving cryogenic temperatures. For semiconductors, theoretical predictions have shown their potential to be cooled to as low as 50 K starting from room temperature,<sup>20</sup> but experimental success is yet to be achieved due to some serious challenges to be overcome.

The basic principles of laser cooling and its thermodynamic validity provided motivation for the above mentioned experiments. Except for these, more detailed theoretical analysis achieved very limited progress, compared to the rapid improvements of laser cooling experiments. This is mainly due to very complicated physical mechanisms under the laser cooling process. Lamouche

\* Author to whom correspondence should be addressed.

<sup>†</sup> Present address: School of Mechanical Engineering, Purdue University, West Lafayette, IN 47907, USA.

considered the temperature dependence of cooling efficiency.<sup>21</sup> By analyzing the temperature dependence of fluorescence and absorption spectra of  $\text{Yb}^{3+}:\text{ZBLAN}$ , they concluded that cooling would decrease with decreasing temperature. Fernandez et al.<sup>12</sup> used the Fermi golden rule to interpret their experimental results, by assuming that the absorption is dominated by the phonon-assisted process. The absorption rate  $\dot{\gamma}_{e,a}$  is given by

$$\dot{\gamma}_{e,a} = \sum_f \dot{\gamma}_{e,i-f} = \frac{2\pi}{\hbar} \sum_f |M_{fi}|^2 \delta(\hbar\omega_{ph,i} + \hbar\omega_p - \hbar\omega_{e,g}) \quad (1)$$

where  $\hbar$  is the Planck constant divided by  $2\pi$ ,  $M_{fi}$  is the interaction matrix element,  $\omega_{ph,i}$  is the incident frequency,  $\omega_p$  is the phonon energy, and  $\hbar\omega_{e,g}$  is the energy gap between the two electronic levels. The  $\delta$  function guarantees the energy conservation, that the sum of the pumping photon energy and the phonon energy should be equal to the electronic gap energy. Recently we have used the Fermi golden rule to decouple various limiting factors, aiming to develop an atomic level understanding.<sup>22</sup> The absorption rate is ultimately expressed as<sup>22</sup>

$$\dot{\gamma}_{e,a} = \frac{2\pi}{\hbar} \frac{(\mathbf{e}_\alpha \cdot \boldsymbol{\mu}_{e,21})^2}{2\varepsilon_0} \frac{|a_{i-p}|^2}{2\rho u_p^2} \frac{D_p(E_p) f_p^o(E_p)}{E_p} \hbar\omega_{ph,i} \frac{f_{ph}}{V_s} \quad (2)$$

where  $\boldsymbol{\mu}_{e,21}$  is the electric transition dipole moment between the upper level 2 and the lower level 1,  $\mathbf{e}_\alpha$  is the polarization vector of the electromagnetic waves,  $a_{i-p}$  is the ion(electron)-phonon coupling factor,  $\varepsilon_0$  is the electric permittivity of vacuum,  $\rho$  is the density,  $u_p$  is the speed of sound,  $D_p$  is the phonon density of states,  $E_p$  is the phonon energy, and  $V_s$  is the volume of the solid. Based on this expression, one finds that the cooling performance is limited by the populations of the three carriers and their couplings. The nanostructure was proposed to be capable of enhancing the carrier populations. However, an understanding to link the photon-electron and ion-phonon coupling mechanisms to the atomic structure, especially in the quantitative level, is still lacking in spite of their fundamental importance. This is the primary goal of the study presented here.

In the sections followed, a  $\text{Ti}[(\text{H}_2\text{O})_6]^{3+}$  complex will be used as the model system, rather than a periodic solids, primarily because the excited states of a finite system is much simpler to analyze while the physics is still preserved. This work can be extended to solids when excited states for ion-doped periodic systems become more tractable with *ab initio* calculations. The roles played by the electron-photon and electron-phonon couplings in laser cooling of solids will be discussed, and an *ab initio* approach to calculate these coupling rates using their atomic structure will be developed. The electron-photon and electron-phonon coupling rates are attempted using *ab initio* calculations. The electron-photon coupling is routed in the transition dipole moment which connects the ground and excited

states. The wavefunctions are calculated and the transition dipole moment is determined using its definition solely. The vibrational frequencies and energy minima are calculated for normal modes, using the small-displacement approach. These are used along with the electronic wavefunctions, in the Fermi golden rule, to derive the nonradiative decay rates. Finally the the roles of electron-photon and electron-vibration couplings in laser cooling materials selections will be discussed.

## 2. AB INITIO CALCULATIONS OF THE GROUND AND EXCITED STATES

### 2.1. Ground State Geometry Optimization

The calculation in this study is performed using Gaussian 03 Package,<sup>23</sup> with the B3LYP method and the 6-311+G\* basis set. The  $\text{Ti}^{3+}$  ion has a single unpaired electron, which gives a spin multiplicity of 2 for the complex. To avoid SCF convergence problems, a quadratic convergent procedure has been applied. No symmetry restriction was prescribed at the start of the calculation, and the optimized geometry converges to the  $D_{3d}$  all vertical symmetry, as shown in Figure 1. This symmetry is lower than the  $O_h$  point group and higher than  $C_i$ . The calculated Ti—O bond length is 2.07 Å, which agrees well with the experimental value 2.03 Å (Ref. [24]) and previously reported ground-state calculations on this complex.<sup>25,26</sup>

### 2.2. Excited State Calculations

Excited state calculations have previously been performed on the  $\text{Ti}[(\text{H}_2\text{O})_6]^{3+}$  complex using a multi-reference

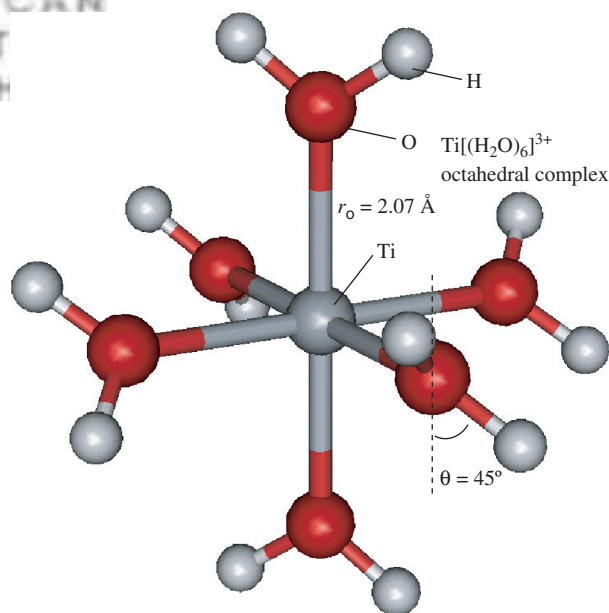


**Fig. 1.** (Color online) The optimized geometry of the ground state  $\text{Ti}[(\text{H}_2\text{O})_6]^{3+}$  (hydrated titanium) complex.

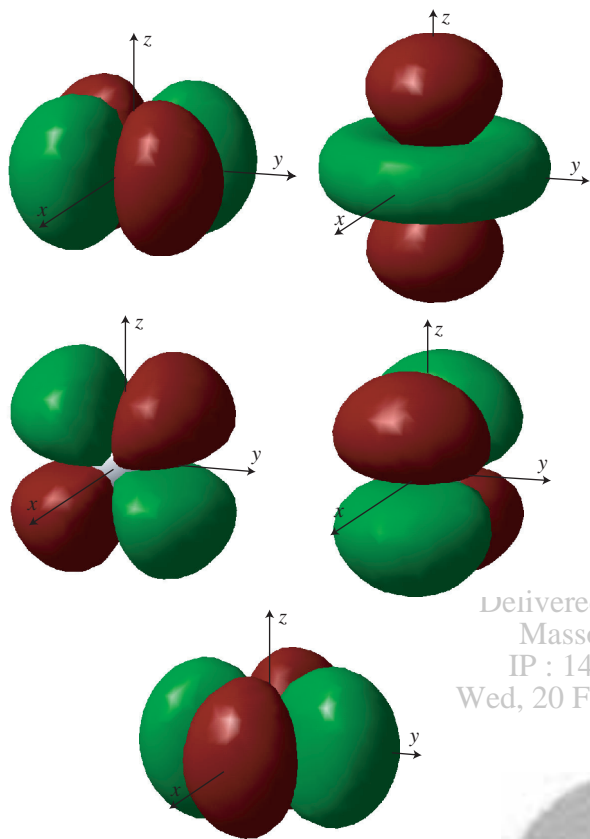


Fig. 2. (Color online) The 3d orbitals of a single  $Ti^{3+}$  ion.

single- and double-excitation CI (MR-SD-CI) method.<sup>25</sup> Here we use the time-dependent density functional theory (TDDFT), which is regarded as the most accurate method for excited states, to calculate the energy levels for the complex at the ground state equilibrium geometry. These energy levels can be viewed as evolved from those of a free standing  $Ti^{3+}$  ion, which has 5 degenerate  $d$  levels, with the orbitals shown in Figure 2. As the ion is put into an octahedral crystal field by the six surrounding oxygen

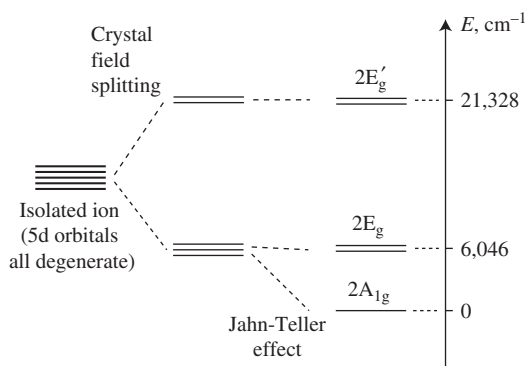


Fig. 3. (Color online) The formation of the energy levels of the  $Ti[(H_2O)_6]^{3+}$  complex at the ground state equilibrium geometry. The  $Ti-O$  bond length is  $r_o = 2.07 \text{ \AA}$ . The energy multiplets lifted by the crystal field and the Jahn-Teller effect are shown.

atoms, the levels are split into two groups, three levels for the ground state and two levels for the excited state. The Jahn-Teller effect further splits the ground state into two multiplets, with an energy gap of  $6,046 \text{ cm}^{-1}$ . The Jahn-Teller theorem states that any complex occupying an energy level with electronic degeneracy is unstable against a distortion that removes that degeneracy in first order. The vibronic coupling of ions in solids can cause a local distortion of the lattice in which the atoms move in the direction of normal-mode displacement to lift the electronic degeneracy. A new equilibrium position is achieved in which the local symmetry is lower than the point-group symmetry of the crystal. Here for the  $Ti[(H_2O)_6]^{3+}$  complex the symmetry is lowered from the  $O_h$  to  $C_j$ . The evolution of the energy levels is shown in Figure 3.

### 3. ELECTRON-PHOTON COUPLING AND THE RADIATIVE DECAY RATE

#### 3.1. Transition Dipole Moment

A photon can be absorbed by an ion if the coupling factor  $e_\alpha \cdot \mu_e$  is nonzero (i.e., they are not orthogonal), where  $e_\alpha$  is the polarization vector of the electromagnetic field, and  $\mu_e$  is the effective transition dipole moment of the ion. The transition dipole moment is defined as a quantum mechanical spatial integral of the classical dipole moment  $e_e r$ , i.e.,

$$\mu_{e,21}^2 = \sum_{m_1} |\langle 1m_1 | e_e r | 2m_2 \rangle|^2 \quad (3)$$

where,  $e_e$  is the electron charge,  $r$  is the position vector,  $m_1$  is the sublevels of the ground state 1, and  $m_2$  is the sublevels of the excited state 2. Note that  $\mu_{e,21}$  must be independent of  $m_2$ . Otherwise, the different  $m_2$  levels would have different transition dipole moments and radiative lifetimes, which are not possible in an isotropic environment.

The wavefunctions  $|1m_1\rangle$  and  $|2m_2\rangle$  are calculated with Gaussian and are shown in Figure 4. The *ab initio* calculations showed that the energies of the orbitals below the HOMO (highest occupied molecular orbital) are approximately the same for the ground and the excited electronic states, so that the differences of the state energies can be discussed with these singly occupied molecular orbital

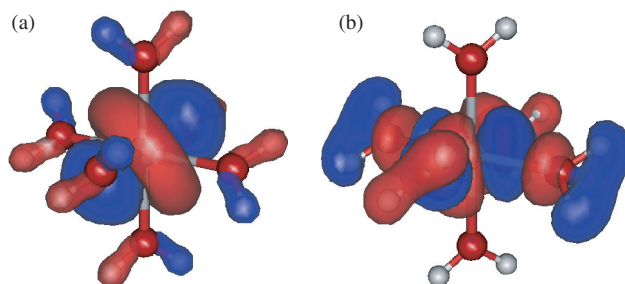


Fig. 4. (Color online) Calculated wavefunctions of the ground and excited states.

(SOMO) energies. The ground state is mainly composed of the  $3d_{z^2}$  orbital, and the excited state is dominated by the  $3d_{x^2-y^2}$  orbital. The transition dipole moment between a sublevel  $m_1$  of the ground state and a sublevel  $m_2$  of the excited state is then calculated by

$$\boldsymbol{\mu}_{e, \text{sub}} = |\langle 1m_1 | e_e \mathbf{r} | 2m_2 \rangle| \quad (4)$$

which gives 0.002 Debye ( $7.319 \times 10^{-33}$  C·m). This value is very small, indicating that the ground state and excited state have very similar symmetry properties.

Due to the strong electron-phonon coupling in  $\text{Ti}^{3+}$  systems, the ground state has many vibrational sublevels. If we assume there are  $N$  sublevels and each has a similar transition dipole moment, then the total transition dipole moment becomes

$$\boldsymbol{\mu}_{e, 21}^2 = N \boldsymbol{\mu}_{e, \text{sub}}^2 \quad (5)$$

where  $N$  will be determined by fitting to experimental data in the following section.

### 3.2. Radiative Lifetime and Absorption Cross Section

A variety of parameters can be used to describe the strength of the light-electron interaction, such as the Einstein  $A$  and  $B$  coefficients, the radiative lifetime  $\tau_r$ , the oscillator strength, the absorption cross section, etc. These parameters are all governed by a fundamental atomistic scale quantity: the transition dipole moment. For example, the Einstein  $A$  coefficient (equivalent to the radiative decay rate  $\dot{\gamma}_r$ ) and the radiative lifetime  $\tau_r$  are related to the transition moment by<sup>27</sup>

$$A_{21} = \dot{\gamma}_r = \frac{\omega_{e,g}^3}{3\pi\epsilon_0\hbar c^3} |\boldsymbol{\mu}_{e, 21}|^2 \quad (6)$$

$$\tau_r = \frac{1}{\dot{\gamma}_r} = \frac{3\pi\epsilon_0\hbar c^3}{\omega_{e,g}^3} \frac{1}{|\boldsymbol{\mu}_{e, 21}|^2} \quad (7)$$

where  $\epsilon_0$  is the electric permittivity in vacuum, and  $\hbar$  is the Planck constant divided by  $2\pi$ . The lifetime of Ti:sapphire was measured by spectroscopy experiments to be  $3 \mu\text{s}$ .<sup>28, 29</sup> By substituting Eq. (5) into (7), the number  $N$  can be determined to be  $N = 25,806$ , indicating that the vibronic effect of Ti doped systems is significant. The value of  $A_{21}$  is then  $3.33 \times 10^5$  1/s.

The absorption cross section is related to the  $A$  coefficient by<sup>27</sup>

$$\sigma_a(\omega) = \frac{1}{4} \left( \frac{2\pi c}{\omega_{e,g}} \right)^2 g(\omega) A_{21} \quad (8)$$

where  $g(\omega)$  is the line shape function which satisfies the normalization condition

$$\int_{-\infty}^{+\infty} g(\omega) d\omega = 1 \quad (9)$$

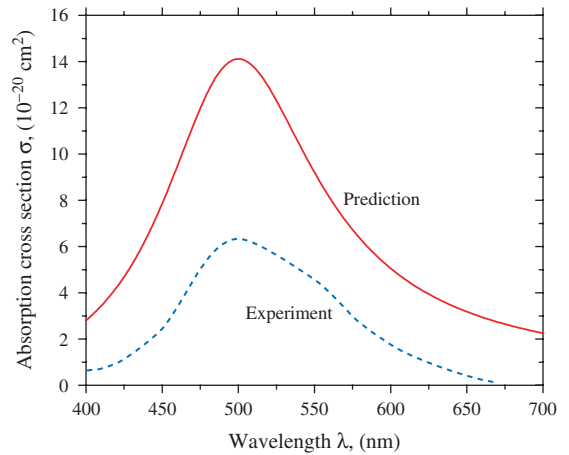


Fig. 5. (Color online) Calculated and experimental absorption spectra.

The line shape function can often be assumed in the form of a Lorentzian function

$$g(\omega) = \frac{1}{\pi} \frac{\frac{1}{2}\Gamma}{(\omega - \omega_0)^2 + (\frac{1}{2}\Gamma)^2} \quad (10)$$

This function has a peak at  $\omega = \omega_0$ , and a full width at half maximum  $\Gamma$ . The  $\text{Ti}^{3+}$ :sapphire material has very broad absorption and emission spectra due to the vibrational sublevels. The absorption spectrum is centered at  $\lambda_0 = 500$  nm, and the full width at half maximum is 130 nm (starts at 450 nm and ends at 580 nm).<sup>30</sup> From these we get  $\omega_0 = 3.77 \times 10^{15}$  rad/s, and  $\Gamma = 9.39 \times 10^{14}$  rad/s. Using Eq. (10) in Eq. (8), the absorption cross section is readily predicted, and the results are shown in Figure 5. The predicted results compare well with the experimental values in Ref. [30], considering the uncertainties in experiments due to impurities, defects, etc.

## 4. ELECTRON-VIBRATION COUPLING

The atoms in a solid are never completely at rest. The thermal vibrations of the atoms modulate the local crystal field at the site of an optically active ion. This modulation can have several types of effects on the optical properties of the doped ion. For example, it can modulate the position of the electronic energy levels, leading to a broadening and shifting in peak position of the spectral transition. Also it can cause transitions to occur between electronic energy levels accompanied by the absorption or emission of vibrational energy but with or without the emission or absorption of photons.

### 4.1. Normal Mode Analysis for Vibrations

The coupling of an electron to a specific vibrational mode is essentially the change of the electronic property in response to the lattice displacement along that vibrational mode. The normal vibrational modes of the  $\text{Ti}[(\text{H}_2\text{O})_6]^{3+}$

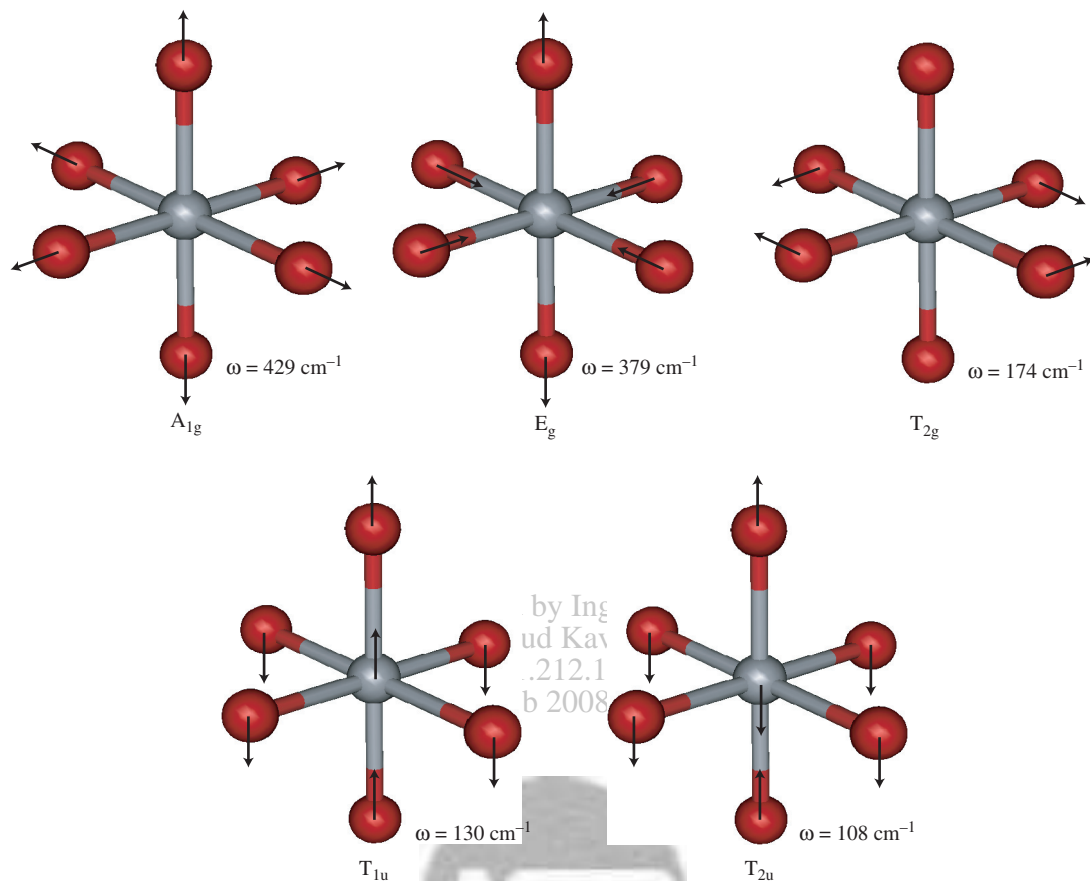


**Fig. 6.** (Color online) The vibrational normal modes along with the frequencies of the  $\text{Ti}[(\text{H}_2\text{O})_6]^{3+}$  complex.

complex can be conveniently calculated with Gaussian, after the geometry is optimized. Among all calculated modes, we only consider those which are also observed for the octahedral  $\text{TiO}_6$  core. The modes due to the hydrogen atoms only do not contribute significantly to the electron-phonon coupling, since these modes are screened by the more inner oxygen atoms. The vibrational normal modes and frequencies are shown in Figure 6.

#### 4.2. Configuration Coordinate Diagram

Configuration coordinate diagram is often used to describe transitions between electronic transitions coupled to vibrations. It depicts the variation in the electronic energy levels with respect to the displacement of the normal vibrational coordinate away from its equilibrium position. Here since the vibration modes due to hydrogen atoms have very little effect on the energy level of the  $\text{Ti}^{3+}$  ion, we only concern the vibration of the octahedral  $\text{TiO}_6$  core. For these modes the hydrogen atoms move rigidly with the oxygen atoms.

The configuration coordinate diagram is obtained by calculating the energy levels with respect to the normal coordinate of a specific vibrational mode. Shown in Figure 7 is the configuration coordinate diagram corresponding to the  $A_{1g}$  normal mode. Five levels resulted from the  $3d$  orbitals

are shown. As discussed in Figure 3, we have the ground state  ${}^2A_{1g}$ , the first excited state  ${}^2E_g$  which is composed of two nearly degenerate levels, and the second excited state  ${}^2E'_g$  which is also composed of two nearly degenerate levels. The transition between the  ${}^2A_{1g}$  and  ${}^2E'_g$  levels is very important in lasers and luminescent applications, and therefore we will only concern these two states in the

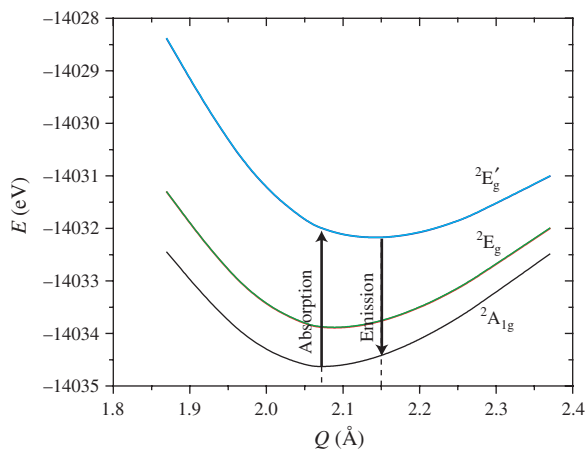


**Fig. 7.** (Color online) Configuration coordinate diagram corresponding to the  $A_{1g}$  normal mode.

following sections. As shown in the figure, the potential energy minimum for the excited state is shifted to the right to that of the ground state, as expected. This shift leads to the well-known Stokes shift in the emission wavelength. For the excited state, the electron is normally farther away from its nuclei than the ground state, repelling the surrounding oxygen atoms. As the result, the equilibrium Ti—O bond length for the excited state becomes longer than the ground state, which again leads to a smaller force constant and vibrational frequency—the curvature for the excited state is flatter than that for ground state. To take into account the modifications of both normal coordinates and frequencies between the electronic states, we can express them in general as follows:

$$Q' = Q + d \tag{11}$$

$$\omega'_s = \omega_s(1 - \rho) \tag{12}$$

where  $d$  is the shift of the energy minimum, and  $\rho$  is the percentage of the frequency shift. As will be seen later, only these normal modes which have modifications in either normal coordinates or frequencies between the electronic states concerned, can contribute to the radiationless transition probability. The Huang-Rhys coupling factor  $S_s$  for a particular phonon mode  $s$  was found to be written as

$$S_s = \frac{M\omega_s d^2}{2\hbar} \tag{13}$$

where  $M$  is the mass of the vibrating atom, the O atom here.

### 4.3. Nonradiative Transition Rates

For electron-vibration coupling, only those normal modes which have modifications in either normal coordinates or frequencies between the electronic states concerned, can contribute to the nonradiative transition probability.

In the Born-Oppenheimer approximation, the system wavefunction  $\psi$  is presented as<sup>30</sup>

$$\psi_{i,\nu}(r, Q) = \phi_i(r, Q)\theta_{i,\nu}(Q) \tag{14}$$

where  $\theta_{i,\nu}(Q)$  is the vibrational wavefunction at a nuclei normal coordinate  $Q$ , and  $\phi_i(r, Q)$  is the electronic wavefunction for a fixed position of the nuclei. This implies that the motion of the electron is very rapid compared to the nuclei motion. The Hamiltonian  $H$  for the entire system can be chosen as:

$$H = T(Q) + H_i(r) + H_i^{ep}(Q) \tag{15}$$

where  $T$  is the kinetic-energy operator of all nuclear motions,  $H_i(r)$  is the electronic-energy operator for electronic states, and  $H_i^{ep}(Q)$  is the electron-lattice interaction potential. In the adiabatic approximation,  $\phi_i(r, Q)$

and  $\theta_{i,\nu}(Q)$  are solutions of the following Schrödinger equations:

$$[H_i(r) + H_i^{ep}(Q)]\phi_i(r, Q) = U_i(Q)\phi_i(r, Q) \tag{16}$$

$$[T(Q) + U_i(Q)]\theta_{i,\nu}(Q) = E_{i,\nu}(Q)\theta_{i,\nu}(Q) \tag{17}$$

where  $U_i(Q)$  is the adiabatic potential of the electronic state at the instantaneous positions  $Q$ , and  $\nu$  signifies the over-all vibrational state of the nuclei. Although  $\psi_{i,\nu}$  is a good approximation for stationary states, it is not stationary in the exact sense, and the whole system oscillates to and fro among various good quantum states of almost the same energy. This should be interpreted as the transition from one electronic state to another, accompanied by a transition in the quantum states of nuclear motion. The perturbation Hamiltonian  $H'$  for the nonradiative transition process is given by<sup>30,31</sup>

$$H'\psi_{i,\nu}(r, Q) = -\frac{\hbar^2}{2M} \sum_s \frac{\partial \phi_i(r, Q)}{\partial Q_s} \frac{\partial \theta_{i,\nu}}{\partial Q_s} - \frac{\hbar^2}{2M} \sum_s \frac{\partial^2 \phi_i(r, Q)}{\partial Q_s^2} \theta_{i,\nu} \tag{18}$$

The nonradiative transition rate  $\dot{\gamma}$  is given by the Fermi Golden Rule,

$$\dot{\gamma}_{nr} = \frac{2\pi}{\hbar} \sum_{\nu, \nu'} p_{i\nu} |\langle f\nu' | H' | i\nu \rangle|^2 \delta(E_{f,\nu'} - E_{i\nu}) \tag{19}$$

where  $p_{i\nu}$  is the distribution function for the Boltzmann population of initial vibrational levels and a  $\delta$  function is used for the density of final states to ensure conservation of energy. Using the electronic and vibrational wavefunctions in Eq. (19), we have

$$\dot{\gamma}_{nr} = \frac{2\pi}{\hbar} \sum_{\nu, \nu'} P_{i\nu} \left| \left( -\frac{\hbar^2}{M} \right) \sum_s \left\langle \phi_f \left| \frac{\partial \phi_i}{\partial Q_s} \right. \right\rangle \times \left\langle \theta_{f\nu'} \left| \frac{\partial \theta_{i\nu}}{\partial Q_s} \right. \right\rangle \right|^2 \delta(E_{f\nu'} - E_{i\nu}) \tag{20}$$

Here the electronic part of the matrix element can be defined as

$$R_s(fi) = -\frac{\hbar^2}{M} \left\langle \phi_f \left| \frac{\partial \phi_i}{\partial Q_s} \right. \right\rangle \tag{21}$$

The derivative represents how sensitive the electronic wavefunction is with respect to the displacement along a particular vibrational mode. This is shown in Figure 8.

Equation (20) has been evaluated by Lin<sup>31</sup> by replacing the  $\delta$  function with an integral, and the final result of the transition probability of the nonradiative decay is

$$\dot{\gamma}_{nr} = \frac{\pi \omega_s}{2\omega_s \hbar^3} |R_s(fi)|^2 \exp \left[ -S_s \coth \frac{\hbar \omega_s}{2kT} \right] \times \left[ \left( \coth \frac{\hbar \omega}{2kT} + 1 \right) \exp(-i\phi' P_i^+) I_{P_i^+} \left( S_s \operatorname{csch} \frac{\hbar \omega}{2kT} \right) + \left( \coth \frac{\hbar \omega}{2kT} - 1 \right) \exp(-i\phi' P_i^-) I_{P_i^-} \left( S_s \operatorname{csch} \frac{\hbar \omega}{2kT} \right) \right] \tag{22}$$

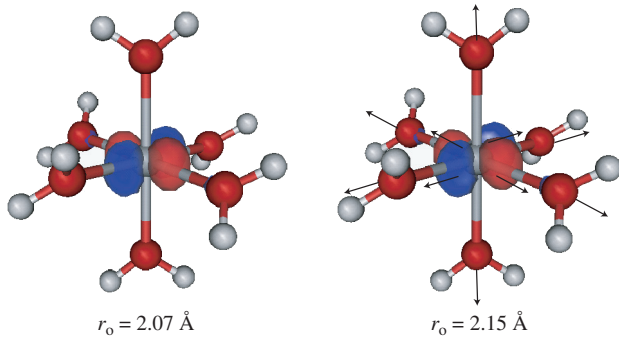


**Fig. 8.** (Color online) The modulation of the excited state wavefunction with respect to the  $A_{1g}$  vibrational mode.

where  $\omega$  is the same as  $\omega_s$ ,  $I_{P_i^+}$  is the  $P_i^+$ th order Bessel function, and  $P_i^+$  and  $P_i^-$  are defined as follows:

$$P_i^+ = \frac{1}{\omega} \left[ -\omega_{ab} - \omega_s + \frac{\rho\omega}{2} \coth \frac{\hbar\omega}{2kT} \right] \quad (23)$$

$$P_i^- = \frac{1}{\omega} \left[ -\omega_{ab} + \omega_s + \frac{\rho\omega}{2} \coth \frac{\hbar\omega}{2kT} \right] \quad (24)$$

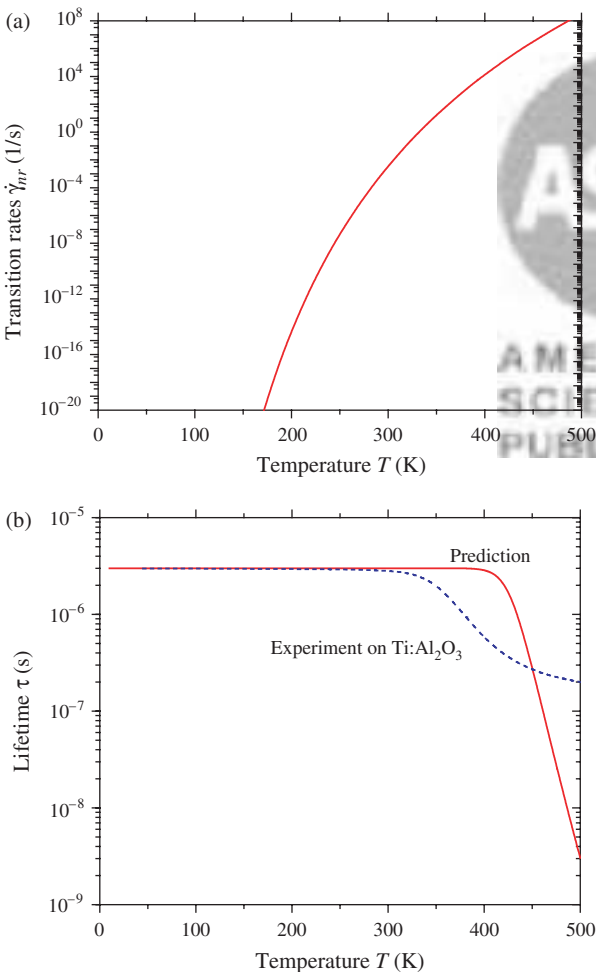


**Fig. 9.** (Color online) (a) The total transition rate with respect to temperature. (b) The lifetime with respect to temperature.

where  $\omega_{ab}$  is the energy gap of the ground and excited states.

Using Eq. (22), the nonradiative decay rate is calculated as a function of temperature, and is shown in Figure 9(a). The total decay rate is the summation of the radiative and nonradiative rates, as

$$\dot{\gamma}_d = \dot{\gamma}_r + \dot{\gamma}_{nr} \quad (25)$$

and the lifetime is given by

$$\tau_d = \frac{1}{\dot{\gamma}_d} \quad (26)$$

The calculated lifetime in this way is shown in Figure 9(b). As seen, at low temperatures, the nonradiative decay rate is negligibly small compared to the radiative decay rate, so that the lifetime remains almost a constant. As the temperature increases, more phonons are activated and involved in the decay process, and the nonradiative decay rate is increasing rapidly. At around 350 K, the nonradiative decay rate becomes comparable or even larger than the radiative decay rate, and the lifetime drops significantly with temperature. At high temperatures, the decay process is dominated by the nonradiative decay.

## 5. DISCUSSIONS AND CONCLUSIONS

Laser cooling cycle is realized in five steps: electron-phonon coupling, phonon-assisted absorption, thermalization in the excited state, electronic decay, and thermalization in the ground state. These steps are shown in Figure 10.

In the above sections the kinetics of laser cooling cycle has been presented, and the time scales of each step are obtained by predictions and measurements, as shown in Figure 11. Four characteristic times are marked in the figure, which are the absorption time, thermalization time at the excited state, lifetime, and the thermalization time at the ground state. The absorption time is the longest in the entire cycle, indicating that the absorption is the bottleneck process that limits the laser cooling performance.

The above theoretical framework can be used to guide the selection of laser cooling materials. Based on Eq. (2), both the electron-photon and the electron-phonon coupling strengths need to be enhanced, to enhance the absorption rate. A negative side effect of the electron-phonon coupling is the nonradiative decay, which leads to heating in the system. However, the operation temperature of laser cooling is no more than the room temperature (300 K), and for this temperature range the nonradiative decay rate is negligibly small. Therefore the electron-phonon coupling can be enhanced without deteriorating the radiative decay process. To enhance the photon-electron coupling, the dopant ion and the host should be selected

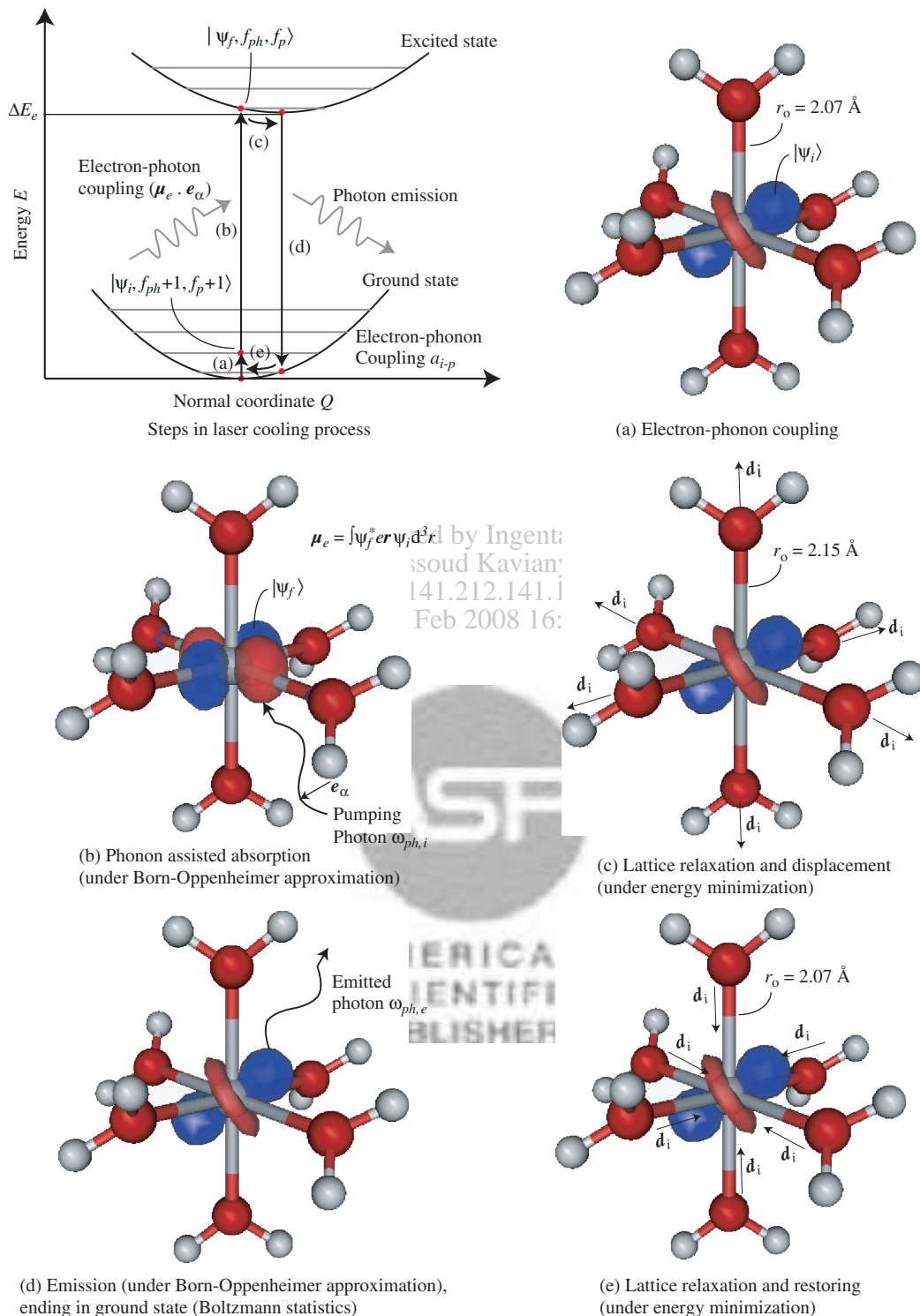
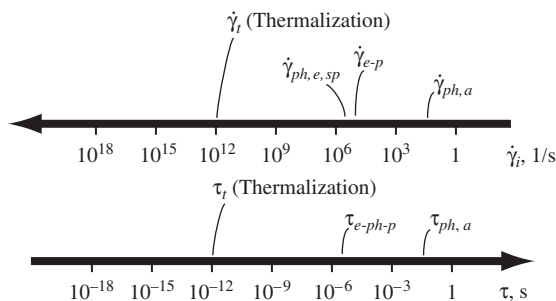


Fig. 10. (Color online) (a) The energy diagram, (b)–(e) five steps in the photon-electron-phonon couplings in the laser cooling cycle.

in the way that the transition dipole moment is large. To enhance the electron-phonon coupling, the electronic wavefunction should be sensitive to vibrations modes, and the modification of vibrational modes before and after transition should be significant. For example, transition metal ions has its valence electrons directly exposed to the

crystal field, unlike rare-earth ions for which the valence electrons are shielded by outer electrons, and as a result, transition-metal doped system has a much larger electron-phonon coupling. The *ab initio* approach developed in this work can be used to guide the selection of laser cooling materials.



**Fig. 11.** (Color online) Transition rates and time scales of each step for laser cooling of solids, for  $\text{Ti}^{3+}:\text{Al}_2\text{O}_3$ . The phonon-assisted absorption process is the slowest and is regarded as the bottleneck of laser cooling of solids.

**Acknowledgments:** The authors would like to thank the valuable discussions or communications with Barry Duniety, Stephen Fahy, James Foresman, Bernd Kallies, Roberto Merlin, Richard Powell, Stephen Rand, Juan F. Rivas, and Anton Van der Ven. Xiulin Ruan acknowledges the financial support through a predoctoral fellowship from the Rackham Graduate School of Studies, the University of Michigan. The financial support of the National Science Foundation through grant CTS-0553651, is also appreciated.

## References

1. P. Pringsheim, *Z. Phys.* 57, 739 (1929).
2. S. Vavilov, *J. Phys. (Moscow)* 9, 68 (1945).
3. S. Vavilov, *J. Phys. (Moscow)* 10, 499 (1946).
4. L. Landau, *J. Phys. (Moscow)* 10, 503 (1946).
5. T. Kushida and J. E. Geusic, *Phys. Rev. Lett.* 21, 1172 (1968).
6. N. Djeu and W. T. Whitney, *Phys. Rev. Lett.* 46, 236 (1981).
7. R. I. Epstein, M. I. Buckwald, B. C. Edwards, T. R. Gosnell, and C. E. Mungan, *Nature* 377, 500 (1995).
8. C. E. Mungan, M. I. Buchwald, B. C. Edwards, R. I. Epstein, and T. R. Gosnell, *Appl. Phys. Lett.* 71, 1458 (1997).
9. X. Luo, M. D. Eisaman, and T. R. Gosnell, *Opt. Lett.* 23, 639 (1998).
10. B. C. Edwards, J. E. Anderson, R. I. Epstein, G. L. Mills, and A. J. Mord, *J. Appl. Phys.* 86, 6489 (1999).
11. T. R. Gosnell, *Opt. Lett.* 24, 1041 (1999).
12. J. Fernandez, A. Mendioroz, A. J. Garcia, R. Balda, and J. L. Adam, *Phys. Rev. B* 62, 3213 (2000).
13. R. I. Epstein, J. J. Brown, B. C. Edwards, and A. Gibbs, *J. Appl. Phys.* 90, 4815 (2001).
14. A. Rayner, M. E. J. Friese, A. G. Truscott, N. R. Heckenberg, and H. Rubinsztein-Dunlop, *Journal of Modern Optics* 48, 103 (2001).
15. C. W. Hoyt, M. P. Hasselbeck, M. Sheik-Bahae, R. I. Epstein, S. Greenfield, J. Thiede, J. Distel, and J. Valencia, *J. Opt. Soc. Am. B* 20, 1066 (2003).
16. B. Heeg, M. D. Stone, A. Khizhnyak, G. Rumbles, G. Mills, and P. A. Debarber, *Phys. Rev. A* 70, 021401 (2004).
17. J. Thiede, J. Distel, S. R. Greenfield, and R. I. Epstein, *Appl. Phys. Lett.* 86, 154107 (2005).
18. S. R. Bowman and C. E. Mungan, *Appl. Phys. B* 71, 807 (2000).
19. A. Mendioroz, J. Fernandez, M. Voda, M. Al-Saleh, R. Balda, and A. J. Garcia-Adeva, *Opt. Lett.* 27, 1525 (2002).
20. M. Sheik-Bahae and R. I. Epstein, *Phys. Rev. Lett.* 368, 247403 (2004).
21. G. Lamouche and P. Lavallard, *J. Appl. Phys.* 84, 509 (1998).
22. X. L. Ruan and M. Kaviany, *Phys. Rev. B* 73, 002619 (2006).
23. M. J. Frisch, G. W. Trucks, H. B. Schlegel, G. E. Scuseria, M. A. Robb, J. R. Cheeseman, J. A. Montgomery, T. Vreven, K. N. Kudin, J. C. Burant, J. M. Millam, S. S. Iyengar, J. Tomasi, V. Barone, B. Mennucci, M. Cossi, G. Scalmani, N. Rega, G. A. Petersson, H. Nakatsuji, M. Hada, M. Ehara, K. Toyota, R. Fukuda, J. Hasegawa, M. Ishida, T. Nakajima, Y. Honda, O. Kitao, H. Nakai, M. Klene, X. Li, J. E. Knox, H. P. Hratchian, J. B. Cross, C. Adamo, J. Jaramillo, R. Gomperts, R. E. Stratmann, O. Yazyev, A. J. Austin, R. Cammi, C. Pomelli, J. W. Ochterski, P. Y. Ayala, K. Morokuma, G. A. Voth, P. Salvador, J. J. Dannenberg, V. G. Zakrzewski, S. Dapprich, A. D. Daniels, M. C. Strain, O. Farkas, D. K. Malick, A. D. Rabuck, K. Raghavachari, J. B. Foresman, J. V. Ortiz, Q. Cui, A. G. Baboul, S. Clifford, J. Cioslowski, B. B. Stefanov, G. Liu, A. Liashenko, P. Piskorz, I. Komaromi, R. L. Martin, D. J. Fox, T. Keith, M. A. Al-Laham, C. Y. Peng, A. Nanayakkara, M. Challacombe, P. M. W. Gill, B. Johnson, W. Chen, M. W. Wong, C. Gonzalez, and J. A. Pople, Gaussian 03, Revision C.02, Gaussian, Inc., Wallingford, CT (2004).
24. P. L. W. Tregenna-Piggott, S. P. Best, M. C. M. O'Brien, K. S. Knight, J. B. Forsyth, and J. R. Pilbrow, *J. Am. Chem. Soc.* 119, 3324 (1997).
25. H. Tachikawa, T. Ichikawa, and H. Yoshida, *J. Am. Chem. Soc.* 112, 982 (1990).
26. B. Kallies and R. Meier, *Inorg. Chem.* 40, 3101 (2001).
27. R. C. Hilborn, *Am. J. Phys.* 50, 982 (1982).
28. R. C. Powell, G. E. Venikouas, L. Xi, and J. K. Tyminski, *J. Chem. Phys.* 84, 662 (1986).
29. P. F. Moulton, *J. Opt. Soc. Am. B* 3, 125 (1986).
30. R. C. Powell, *Physics of Solid-State Laser Materials*, Springer-Verlag, New York (1998).
31. S. H. Lin, *J. Chem. Phys.* 44, 3759 (1966).

Received: 3 November 2006. Accepted: 23 April 2007.